

# Generalized Rotational Susceptibility Studies of Solid $^4\text{He}$

V. Gadagkar · E.J. Pratt · B. Hunt · M. Yamashita ·  
M.J. Graf · A.V. Balatsky · J.C. Davis

Received: 3 February 2012 / Accepted: 20 June 2012 / Published online: 6 July 2012  
© Springer Science+Business Media, LLC 2012

**Abstract** Using a novel SQUID-based torsional oscillator (TO) technique to achieve increased sensitivity and dynamic range, we studied TO's containing solid  $^4\text{He}$ . Below  $\sim 250$  mK, the TO resonance frequency  $f$  increases and its dissipation  $D$  passes through a maximum as first reported by Kim and Chan. To achieve unbiased analysis of such  $^4\text{He}$  rotational dynamics, we implemented a new approach based upon

---

This article is a synthesis of the work first published in Refs. [14] and [15].

V. Gadagkar · E.J. Pratt · B. Hunt · J.C. Davis (✉)  
Laboratory for Atomic and Solid State Physics, Department of Physics, Cornell University, Ithaca, NY 14853, USA  
e-mail: [jcseamusdavis@gmail.com](mailto:jcseamusdavis@gmail.com)

E.J. Pratt  
National Institute of Standards and Technology, 325 Broadway, Boulder, CO 80305, USA

B. Hunt  
Department of Physics, Massachusetts Institute of Technology, Cambridge, MA 02139, USA

M. Yamashita  
Department of Physics, Kyoto University, Kyoto 606-8502, Japan

M.J. Graf · A.V. Balatsky  
Theoretical Division and Center for Integrated Nanotechnologies, Los Alamos National Lab., Los Alamos, NM 87545, USA

J.C. Davis  
Condensed Matter Physics and Materials Science Department, Brookhaven National Laboratory, Upton, NY 11973, USA

J.C. Davis  
Kavli Institute for Theoretical Physics, UC Santa Barbara, Santa Barbara, CA 93016, USA

J.C. Davis  
School of Physics and Astronomy, University of St. Andrews, St. Andrews, Fife KY16 9SS, UK

the generalized rotational susceptibility  $\chi_{4\text{He}}^{-1}(\omega, T)$ . Upon cooling, we found that equilibration times within  $f(T)$  and  $D(T)$  exhibit a complex synchronized ultraslow evolution toward equilibrium indicative of glassy freezing of crystal disorder conformations which strongly influence the rotational dynamics. We explored a more specific  $\chi_{4\text{He}}^{-1}(\omega, \tau(T))$  with  $\tau(T)$  representing a relaxation rate for inertially active microscopic excitations. In such models, the characteristic temperature  $T^*$  at which  $df/dT$  and  $D$  pass simultaneously through a maximum occurs when the TO angular frequency  $\omega$  and the relaxation rate are matched:  $\omega\tau(T^*) = 1$ . Then, by introducing the free inertial decay (FID) technique to solid  $^4\text{He}$  TO studies, we carried out a comprehensive map of  $f(T, V)$  and  $D(T, V)$  where  $V$  is the maximum TO rim velocity. These data indicated that the same microscopic excitations controlling the TO motions are generated independently by thermal and mechanical stimulation of the crystal. Moreover, a measure for their relaxation times  $\tau(T, V)$  diverges smoothly everywhere without exhibiting a critical temperature or velocity, as expected in  $\omega\tau = 1$  models. Finally, following the observations of Day and Beamish, we showed that the combined temperature-velocity dependence of the TO response is indistinguishable from the combined temperature-strain dependence of the  $^4\text{He}$  shear modulus. Together, these observations imply that ultra-slow equilibration of crystal disorder conformations controls the rotational dynamics and, for any given disorder conformation, the anomalous rotational responses of solid  $^4\text{He}$  are associated with generation of the same microscopic excitations as those produced by direct shear strain.

**Keywords** Supersolid helium · Generalized rotational susceptibility · Superglass · Torsional oscillator

## 1 Introduction

Solid  $^4\text{He}$  is a bosonic crystalline material that is a candidate to become a supersolid at low temperature [1–7]. Studies using high-Q torsional oscillators (TO) containing solid  $^4\text{He}$  [8–17] have revealed that the TO resonant angular frequency of rotation  $\omega$  increases rapidly below both  $T \sim 250$  mK and maximum TO rim-velocity  $V \sim 10^{-4}$  ms $^{-1}$ , perhaps as if superfluid inertia becomes decoupled from the container below a critical [18] temperature  $T_c$  and velocity  $V_c$ . Moreover, these TO resonant frequency increases [8–16] are reported to be greatly diminished by blocking the TO annulus [9, 17], as if due to reconnection of that inertia. Features in the specific heat capacity ascribed to a supersolid phase transition [19, 20] or disorder-induced dynamic crossover [21] also occur in this same temperature range.

Nevertheless the phenomenology of this solid also contains many unexpected effects. In DC mass-flow studies, the maximum mass-current densities are several orders of magnitude smaller than those implied by the TO experiments [22–27] and are observed at temperatures far higher than those characteristic of the Kim and Chan effects [23–26]. Experiments in which the  $^4\text{He}$  solid is annealed near the melting temperature with the objective of diminishing any crystal disorder have also shown that the maxima in  $df/dT$  and  $D$  can be greatly reduced within the same sample

[10, 23, 28–31]. Moreover, the temperature dependence of the resonance frequency  $f(T)$  of TO's containing solid  $^4\text{He}$  [8–16] is also very similar to that of its shear modulus  $\mu(T)$  [32] and, coincident with the maximum rates of increase of  $f(T)$  and  $\mu(T)$  are unexplained maxima in TO dissipation [9–11, 13, 14] and shear-dissipation [32, 33], respectively. Finally, the increased values of both  $f$  and  $\mu$  at lowest temperatures are extinguished by increasing TO maximum rim velocity [8–13, 16] or shear strain  $\varepsilon$  [32, 34], respectively. A simple transition to a supersolid appears, at present, to be inconsistent with all these phenomena.

A number of different classes of theoretical models have been proposed to explain the complex rotational dynamics observed for solid  $^4\text{He}$ . The first is a basic supersolid in which Bose-Einstein condensation of vacancies produces a superfluid component interpenetrating the crystal [1–7]. The second class describes an incipient supersolid lacking long range quantum phase coherence [35, 36]. A third class of model is that nanoscale heterogeneous superfluidity can be generated by specific types of crystalline disorder [14, 37–43]. Finally, there are also non-superfluid models in which solid  $^4\text{He}$  contains a population of inertially active crystal excitations [44–49] whose relaxation time  $\tau$  lengthens smoothly with falling  $T$ . These excitations are proposed variously to be a dynamical network of pinned dislocations [32, 33, 44, 49–52], atomic-scale tunneling two-level systems [21, 48, 53], or the glassy response of defects distributed throughout the solid [45–47]. All inertially active excitation models have the property that, as  $\tau(T)$  passes through the condition  $\omega\tau = 1$ , a strong maximum in  $|df/dT|$  and  $D$  should occur [14, 15, 45–49] even though there is no supersolid  $T_c$  and  $V_c$ .

## 2 Generalized Rotational Susceptibility

An unbiased approach to TO studies of solid  $^4\text{He}$  can be achieved by using the TO rotational susceptibility  $\chi(\omega, T) = \theta(\omega, T)/\Gamma(\omega)$  [45–47]. Here  $\theta(\omega, T)$  represents the amplitude of angular displacement as a function of  $\omega$  and  $T$  in response to a constant magnitude harmonic torque  $\Gamma(\omega)$ . It can be shown that [45–47]

$$\chi^{-1}(\omega, T) = K - I\omega^2 - i\gamma\omega - \chi_{4\text{He}}^{-1}(\omega, T) \quad (1)$$

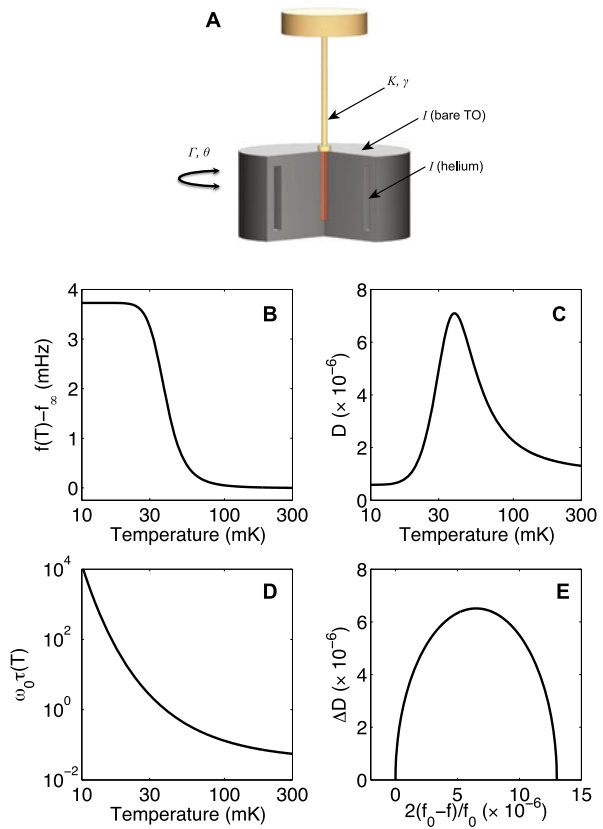
describes the properties of the bare TO plus the ‘back action’ of the solid  $^4\text{He}$  through its complex rotational susceptibility  $\chi_{4\text{He}}^{-1}(\omega, T) = \text{Re}(\chi_{4\text{He}}^{-1}) + i \text{Im}(\chi_{4\text{He}}^{-1})$  [46],  $I$  is the combined moment of inertia of the TO plus  $^4\text{He}$  at zero-temperature,  $K$  is the torsional spring constant, and  $\gamma$  is the TO damping constant (see Fig. 1A).

These concepts can be made concrete by considering, for example, a classic (Debye) form for the rotational susceptibility  $\chi_{4\text{He}}^{-1}(\omega, T)$  [45–47] that describes the freeze-out of an ensemble of excitations whose relaxational time-constant  $\tau(T)$  increases with decreasing  $T$

$$\chi_{4\text{He}}^{-1}(T) = g/(1 - i\omega_0\tau(T)) \quad (2)$$

(for a discussion of the Debye form with a distribution of activation energies, see Ref. [33]). For solid  $^4\text{He}$ ,  $g/\omega_0^2$  would then represent the rotational inertia associated

**Fig. 1** The generalized rotational susceptibility approach to studying torsional oscillator dynamics. (A) Schematic of a torsional oscillator containing solid <sup>4</sup>He with the various parameters appearing in Eq. (1) of the main text. The (B) frequency shift predicted by the Debye susceptibility (Eq. (4a)) for (C) dissipation (Eq. (4b)) obtained by fitting to data. The ratio of the imaginary to the real part of the Debye susceptibility yields the (D) relaxation time (Eq. (5)). The (E) Davidson-Cole plot of the Debye susceptibility (Eq. (6)) is a *semicircle* (Color figure online)



with the relevant excitations, and the components of inertial and dissipative ‘back action’ on the TO at resonance  $\omega_0$  are given respectively by

$$\text{Re}[\chi_{4\text{He}}^{-1}(T)] = \frac{g}{1 + \omega_0^2 \tau^2} \tag{3a}$$

$$\text{Im}[\chi_{4\text{He}}^{-1}(T)] = \frac{g\omega_0\tau}{1 + \omega_0^2 \tau^2}. \tag{3b}$$

As is always the case with such  $\omega\tau = 1$  models, when  $\text{Re}(\chi_{4\text{He}}^{-1})$  changes due to the  $\tau(T)$  term, then  $\text{Im}(\chi_{4\text{He}}^{-1})$  must always change in a quantitatively related fashion. Such changes would be measurable because (see Fig. 1B, 1C), for a high-Q TO containing solid <sup>4</sup>He governed by Eq. (2)

$$\frac{2(f_0 - f(T))}{f_0} = \frac{1}{I\omega_0^2} \text{Re}[\chi_{4\text{He}}^{-1}(T)] \tag{4a}$$

$$D(T) - D_\infty = \frac{1}{I\omega_0^2} \text{Im}[\chi_{4\text{He}}^{-1}(T)] \tag{4b}$$

where  $f_0$  is the frequency at lowest temperature and  $D_\infty$  is the dissipation far above  $T^*$ , and  $D(T) = Q^{-1}(T) - Q^{-1}(T \rightarrow \infty)$  is the inverse contribution to the

TO quality factor  $Q$  from the solid  $^4\text{He}$  [45–47]. Moreover for the susceptibility of Eq. (2)

$$\frac{\text{Im}(\chi_{^4\text{He}}^{-1})}{\text{Re}(\chi_{^4\text{He}}^{-1})} = \frac{D(T)f(0)}{2(f(0) - f(T))} = \omega_0\tau(T) \quad (5)$$

(see Fig. 1D) so that access to  $\tau(T)$  of the microscopic excitations is therefore possible, at least in principle, from measurements of  $\text{Re}(\chi_{^4\text{He}}^{-1})$  and  $\text{Im}(\chi_{^4\text{He}}^{-1})$ .

A well defined characteristic temperature  $T^*$  for any such susceptibility occurs when  $\omega_0\tau(T^*) = 1$ . Both the  $f(T)$  slope and the dissipation  $D(T)$  of a physically plausible susceptibility achieve their respective maxima when the temperature is very close to  $T^*$ . Figures 1B, C are examples of this, using Eq. (3a), (3b) the susceptibility in Eq. (2) and the  $\tau(T)$  in Fig. 1D. This  $T^*$  is a very different concept to that of a critical temperature, since it is not related to a thermodynamic phase transition but is, instead, the temperature at which a probe frequency and the microscopic relaxation rate are matched:  $\omega_0\tau(T) = 1$ .

A common tool to illuminate the relationship between the real and imaginary components of such a susceptibility is a direct plot of  $\text{Im}(\chi)$  vs.  $\text{Re}(\chi)$  in the complex plane [54, 55]. When used in the context of the dielectric susceptibility  $\varepsilon$  of classical glasses or polarized liquids, this is called a Cole-Cole or Davidson-Cole (D-C) plot [54, 55] where it is the locus of points  $(\text{Re}[\varepsilon], \text{Im}[\varepsilon])$  which is plotted with the implicit control parameter being typically the measurement frequency  $\omega$ . In high- $Q$  TO experiments, by contrast, the measurement frequency is fixed at the resonant frequency and response of the system is varied by changing  $T$ . The analogous plot would then be the locus of points  $(\text{Re}[\chi^{-1}], \text{Im}[\chi^{-1}])$ , and it should reveal characteristics of the underlying physical mechanism; e.g. deviations from the Debye susceptibility appear as prominent geometric features in the D-C plot. In the case of the rotational susceptibility of the TO-helium system, the D-C plot also eliminates the need for specific models of the relaxation time  $\tau(T)$ . Specifically, the susceptibility,  $\chi_{^4\text{He}}^{-1}(\omega, T) = g/(1 - i\omega_0\tau(T))$ , generates a semicircle (see Fig. 1E) centered on  $X = \text{Re}[\chi_{^4\text{He}}^{-1}] = g_0/2$  with radius  $g_0/2$ , as can be seen by eliminating  $\omega_0\tau$  from Eq. (3a) and (3b). One finds that  $(X - g_0/2)^2 + Y^2 = (g_0/2)^2$ , where  $Y = \text{Im}[\chi_{^4\text{He}}^{-1}]$ . The natural abscissa and ordinate for a Davidson-Cole plot for TO studies are:

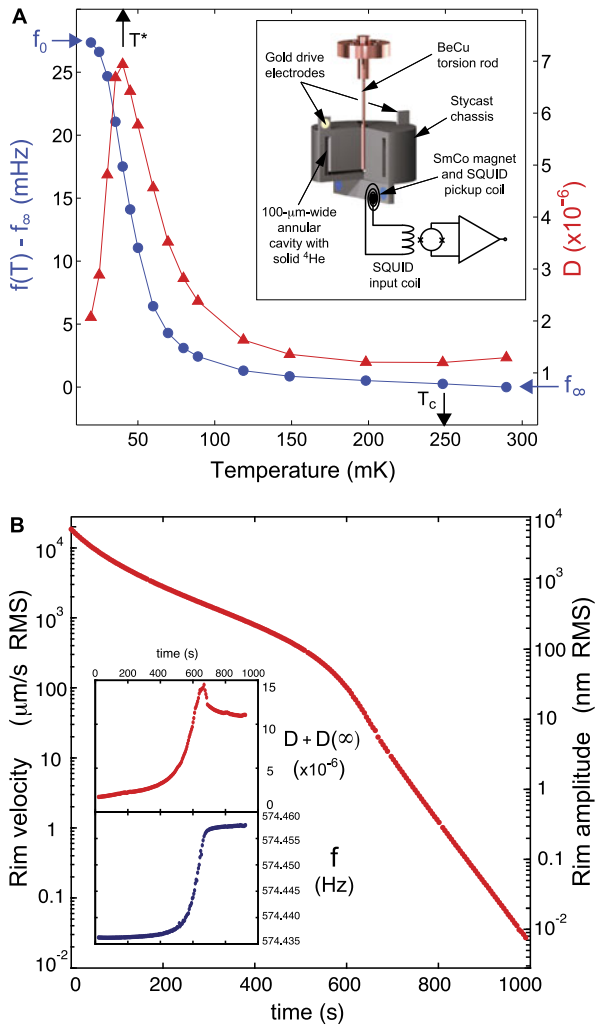
$$\Delta D \text{ vs. } \frac{2\Delta f}{f_0}, \quad (6)$$

where  $\Delta D = D(T) - D_\infty$  and  $\Delta f = f_0 - f(T)$ .

### 3 SQUID-Based High-Resolution Torsional Oscillator

Our main development in solid helium TO techniques was the introduction of a superconducting quantum interference device (SQUID)-based displacement sensor. Such sensors have been used to study aspects of superfluid helium too sensitive to be otherwise detected, such as phase slippage and the Josephson effect in  $^3\text{He}$  and  $^4\text{He}$  [56, 57], and were originally invented for gravity wave detectors. In our experiments,

**Fig. 2** (A) The resonant frequency shift  $f(T) - f_\infty$  (blue circles) and dissipation  $D(T) \equiv Q^{-1}(T)$  (red triangles) for our TO-solid  $^4\text{He}$  system. Indicated with black arrows are  $T^*$ , the temperature at which  $D(T)$  peaks and the slope of  $f(T) - f_\infty$  is maximal, and  $T_c$ , the temperature at which a change in  $f(T) - f_\infty$  becomes detectable above the noise. (Inset to A) A schematic of the SQUID-based torsional oscillator (TO). Applying an AC voltage to the drive electrodes rotates the Stycast chassis (containing the solid  $^4\text{He}$  in a 100- $\mu\text{m}$ -wide annular cavity of radius 4.5 mm) about the axis of the BeCu torsion rod. The angular displacement of a SmCo magnet mounted on the TO generates a change in the magnetic flux through the stationary pickup and input coils of a DC-SQUID circuit and thereby a voltage proportional to displacement. (B) A typical Free-Inertial Decay (FID), taken at 47 mK. This was acquired by stabilizing the temperature, driving the oscillator to high amplitude, and then suddenly turning off the AC drive. (Inset to B) The corresponding frequency and dissipation as a function of time during the FID (Color figure online)



we detect the motion of a high-field permanent samarium cobalt (SmCo) magnet attached to the bottom of the TO (see inset to Fig. 2A) by sensing the change in magnetic flux through a nearby stationary pickup coil. The pickup coil is in series with an input coil inductively coupled to the loop of a DC-SQUID; the two coils and the wire connecting them form a superconducting loop. When a moving magnet attached to the TO changes the magnetic flux through the pickup coil, a current is generated in the superconducting loop and therefore in the input coil as well. The resultant magnetic flux is detected by the DC-SQUID. The DC-SQUID is operated in a flux-locked loop [58] and therefore generates an output voltage  $V_{sq}$  proportional to the change in flux  $\Delta\varphi_{sq}$  in the SQUID loop.

The type of SQUID-based sensor used in the earlier studies noted above also used a superconducting circuit to couple flux changes generated by a moving element into a DC-SQUID loop, but the moving element was not a permanent magnet. In that

case, the moving element was a superconducting plane that modified the inductance  $L$  of a nearby pickup coil in a (primary) superconducting loop containing a persistent current  $I$ . Since  $\Delta\Phi = 0$  in a superconducting loop, a change in the inductance due to the moving superconducting plane generated a change in the persistent current  $I_1 \rightarrow I_1 + \delta I_1$ , which could be coupled (via a secondary superconducting loop and a secondary persistent current  $I_2$ ) into the DC-SQUID. For more details about this detection scheme, see [59]. Our novel permanent magnet method has several advantages over the older method. These are related primarily to the simplicity of our circuit. First, the probability of success of either detection scheme is related to the number of superconducting (SC) joints that need to be made between the various superconducting elements in the two circuits. Our new scheme has 6, whereas the older scheme has 9, including two 3-way SC joints. Additionally, the SC joints determine the critical current of the primary superconducting loop  $I_c$  and therefore the maximum persistent current  $I_{\max} = I_c$  that can be injected into the loop. Since the displacement responsivity  $\eta$  of the circuit is directly proportional to the injected current, the responsivity of the displacement sensor can be severely limited by a single low critical current joint. The permanent magnet-scheme is much more reliable in this regard with no loss in responsivity. Second, the injection of the persistent current can be a delicate matter, involving decoupling of the 4 K superconducting circuit and the 300 K current-injection source via a long retractable conduit; the permanent magnet scheme is free of such complications. The DC-SQUID we used [60] has limiting flux sensitivity of  $\sim 5\mu\phi_0/\sqrt{\text{Hz}}$ . The output voltage of the DC-SQUID is proportional to the displacement  $\delta x$  of the magnet, with the proportionality constant called the “responsivity”  $\eta_{sq} : V_{sq} = \eta_{sq}\delta x$ . The responsivity is a function of both the DC-SQUID circuitry and also the particulars of the coupling between the magnet and the pickup coil. For the highest gain settings of the DC-SQUID feedback loop, typical values are  $\eta_{sq} = 1 \text{ V/nm}$  and a displacement noise sensitivity  $\delta x_{\min}$  (corresponding to the flux noise quoted above) below  $10^{-15} \text{ m/Hz}$ . Such responsivity is so high that, for some purposes, we often had to decrease it by moving the coil away from the magnet.

Our solid  $^4\text{He}$  samples were grown from a high-pressure liquid (at 73 bar and 3.3 K) with a nominal  $^3\text{He}$  concentration of 300 ppb by the blocked capillary method, cooling rapidly along the melting curve (approximately 100 minutes from 3.2 K to  $< 1 \text{ K}$ ). Samples typically reach a low-temperature pressure of 39 bar. The samples are formed inside an annular chamber with a cross-section of 100 microns  $\times$  3 mm and radius of 4.5 mm (see inset to Fig. 2A). The torsion rod is made of annealed beryllium copper and the helium sample chambers are made of Stycast 1266 for low inertia. For most of the studies reported here, the resonant frequency at 300 mK is 575.018 Hz for the empty cell and 574.433 Hz for the full cell. The full-cell  $Q$  at 300 mK is  $4 \times 10^5$ . The torsional motion was detected either by a capacitor electrode (used at highest velocities) or via the DC-SQUID based position detector.

Using a TO containing solid  $^4\text{He}$  (Fig. 2A inset) we then measure  $f(T)$  and  $D(T)$  effects in good agreement with other research groups [8–13]. Figure 2 shows the evolution of  $f(T)$  (blue circles) and  $D(T)$  (red triangles) for our typical sample; the change in  $f(T)$  between 300 mK and 10 mK would represent a “supersolid fraction” of 4.8 % if the frequency shift were ascribable to a superfluid decoupling. Our sam-

ples, while formed by the ‘blocked capillary’ procedure and therefore amorphous,<sup>1</sup> are of the type most widely studied in the field [8–13].

#### 4 Ultra-Slow Equilibration

To examine the sample equilibration characteristics of solid  $^4\text{He}$ , we performed the experiment outlined in [14]. The temperature is decreased stepwise from an initial temperature  $T_i$  to a final equilibrium temperature  $T_{eq}$ , and the rapid co-evolution of  $f(t)$  and  $D(t)$  are observed as the thermometers approach  $T_{eq}$ . More importantly, the subsequent changes after the thermometers equilibrate,  $f(t, T_{eq})$  and  $D(t, T_{eq})$ , are measured. While for the initial  $t < t_{eq}$  part of each trace both  $f(T)$  and  $D(T)$  change rapidly with temperature, their slopes change sharply at  $t_{eq}$  indicating that the solid inside the TO maintains thermal equilibrium with the mixing chamber. Above  $T^* \sim 65$  mK which is identified as the point of maximum rate of increase of  $f(T)$  and of the peak in  $D(T)$ , these equilibration rates are independent of temperature and less than 100 s. But below this temperature both equilibration rates begin to increase rapidly on indistinguishable trajectories, indicating that the ultra-slow equilibration processes in  $f$  and  $D$  are intimately linked. Such ultra-slow equilibration processes for solid  $^4\text{He}$  have also been reported in other studies [11, 30, 36, 61–63].

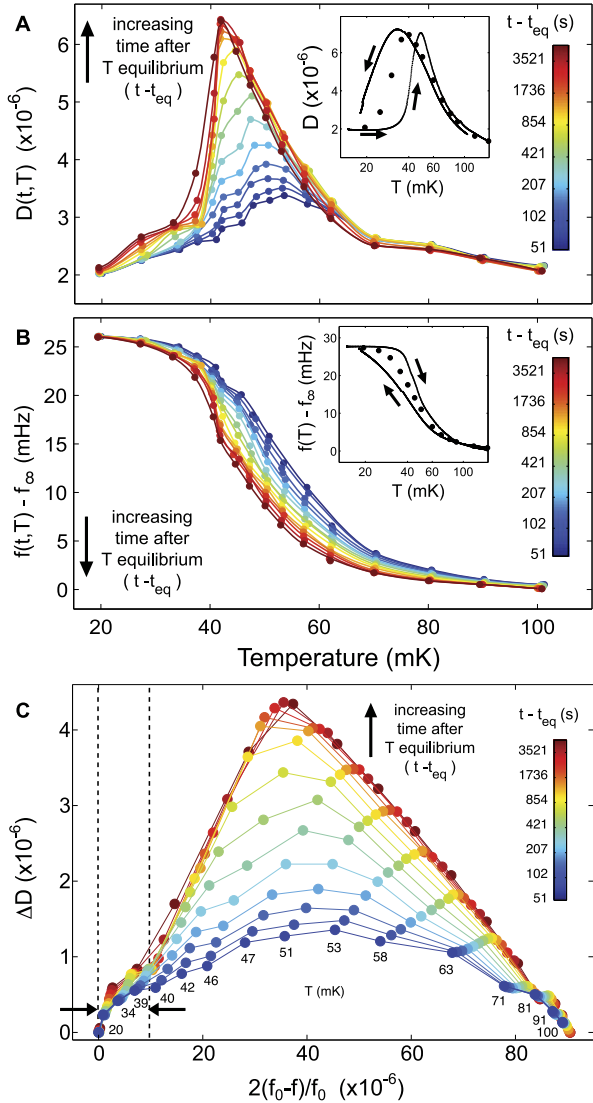
We examine the relationship between the equilibration of dissipation and the frequency shift—as both approach their long-time equilibrium states. In the relevant experiment, the  $^4\text{He}$  sample is cooled to 17 mK and then equilibrated for a time  $t > 20,000$  s to achieve an unchanging state. It is then heated abruptly to a temperature  $T$  and the subsequent equilibration in both  $f(t, T)$  and  $D(t, T)$  are monitored. The resulting time dependence of dissipation  $D(t, T)$  is shown in Fig. 3A. At short times after temperature stabilization, the dissipation increases slightly (dark blue in Fig. 3A). But these dissipative processes are actually very far out of equilibrium. As time passes, the dissipation slowly increases on a trajectory indicated by the transition from the blue line representing  $D(t, T)$  at  $t \sim 50$  s to the dark red line representing  $D(t, T)$  at  $\sim 5000$  s. In the same experiment, the time dependence of  $f(t, T)$  is also measured (Fig. 3B). It differs from that of  $D(t, T)$ ; at shortest times after stabilization at  $T$  the frequency has already changed greatly from its lowest temperature value (Fig. 3B). This means that much of the frequency change responds immediately to the mixing chamber temperature change (and therefore also that rapid thermal equilibrium always exists between the sample and the mixing chamber thermometer—for a detailed discussion of the relevant thermal and mechanical time constants, see Sect. 2 of the supplementary online materials of Ref. [14]). The subsequent equilibration of the remaining component of the frequency shift exhibits an ultra-slow reduction in  $f$  as indicated by the transition from the blue line at  $t \sim 50$  s to the dark red line representing  $t \sim 5000$  s in Fig. 3B.

These data illustrate how the slowing equilibration dynamics within  $D(t, T)$  and  $f(t, T)$  are synchronized in such samples of solid  $^4\text{He}$ . They also imply that thermal

<sup>1</sup>The word ‘amorphous’ (meant to include polycrystalline) is here used to distinguish these samples from single crystals.

**Fig. 3** Measured time evolution of (A)  $D(t, T)$  and (B)  $f(t, T)$  for the abrupt warming experiment described in the text and in [14]. The data are colored circles and the lines are smooth interpolations, intended as guides to the eye. The dark blue lines represent  $D(t, T)$  and  $f(t, T)$  at  $t \sim 50$  s while the dark red lines represent  $D(t, T)$  and  $f(t, T)$  at  $t \sim 5000$  s.

*Insets:* Thermal hysteresis in the dynamical response as shown by the black curves in  $D(T)$  (inset to (A)) and in  $f(T)$  (inset to (B)), with the direction of the temperature change indicated by black arrows. The data indicated by circles were acquired after waiting  $t \gg 5 \times 10^3$  seconds at each temperature as the dynamical response (of Fig. 3A and B) asymptotically approached the infinite-time limit. (C) Time-dependent Davidson-Cole plot. This is a parametric plot of the data shown in Fig. 3A and B—the real and imaginary parts of  $\chi$  (see Eqs. (3a), (3b))—removing the explicit dependence on temperature. The vertical dashed lines indicate the maximum value of  $2(f_0 - f)/f_0$  that would be predicted by the Debye susceptibility (Eq. (2)), given the peak height of  $\Delta D$  (Color figure online)



hysteresis should occur when temperatures are swept faster than the relevant equilibration times in Fig. 3A, B. In the insets to Fig. 3A, B swept-temperature measurements on the same sample show that thermal hysteresis occurs in both  $D(T)$  (inset to Fig. 3A) and  $f(T)$  (inset to Fig. 3B), with their long-time equilibrium values (solid circles) falling within the hysteresis loops, as expected. Such ultra-slow hysteresis effects are also observed in many other solid  $^4\text{He}$  TO studies [11, 36].

Equation (4b) can be fit to the measured  $D(T)$ . Comparison of the resulting prediction from Eq. (4a) for  $f(T)$  to the measured  $f(T)$  shows that a Debye susceptibility is inconsistent with the relationship between  $D(T)$  and  $f(T)$  [14]. Nevertheless, as the equilibration processes of  $D(t, T)$  and  $f(t, T)$  are synchronized (Fig. 3A, B),

there must be an intimate relationship between  $\text{Re}(\chi_{4\text{He}}^{-1})$  and  $\text{Im}(\chi_{4\text{He}}^{-1})$ . To study this relationship following Eq. (6), we make a Davidson-Cole plot  $D(T) - D_\infty$  versus  $\frac{2(f_0 - f(T))}{f_0}$  in Fig. 3C. It reveals that, instantaneously upon warming, the D-C plot is a symmetric elliptical curve, whereas after several thousand seconds the response has evolved into a skewed D-C curve. But the maximum frequency shift expected from the maximum observed dissipation within the Debye susceptibility (vertical dashed lines) is again far too small. Moreover, no temperature equilibration lag between the solid  $^4\text{He}$  sample and the mixing chamber could generate the complex dynamics reported in Fig. 3 because, for any given frequency shift  $f$ , a wide variety of different dissipations  $D$  are observed [14].

## 5 TO Free Inertial Decay Studies

With sufficiently high signal-to-noise ratio and dynamic range, a TO free inertial decay (FID) during which oscillations of large initial amplitude (and maximum rim-velocity  $V$ ) are allowed to decay freely in time during which  $f(V)$  and the dissipation rate  $D(V)$  are measured continuously allows complete mapping of the dynamics in the  $V$ - $T$  parameter space. We introduced this FID approach to TO studies of solid  $^4\text{He}$  [15]. High precision sensing of rotational motions is achieved primarily using the DC-SQUID-based detection (inset to Fig. 2A) of the magnetic flux from a permanent magnet attached to the TO body. From a typical FID (Fig. 2B) at a single temperature  $T$ , the  $f(T, V)$  is measured by using a high-precision frequency counter, and  $D(T, V)$  is determined by the measured rate of energy loss from the TO. The experimental procedure then consists of such measurements over many orders of magnitude in  $V$  during each FID, at a closely spaced sequence of different temperatures  $T$ . Following this approach, the first complete map of rotational susceptibility of a TO containing solid  $^4\text{He}$  throughout the  $V$ - $T$  plane was achieved. The results in Figs. 4A, B show that the frequency increase and dissipation peak are bounded by closely corresponding  $V$ - $T$  contours. This means that the same dissipation peak seen with falling temperature near the proposed supersolid  $T_c$  is found also with diminishing  $V$  in the range of the proposed [8, 9] supersolid  $V_c$ . The highly similar contours of both  $f(T, V)$  and  $D(T, V)$  also reveal that the maxima in  $|df/dT|$  and  $D$  are always linked—as if controlled by some combined function of  $T$  and  $V$ . Similar results were obtained in three distinct samples.

## 6 Analysis of Rotational Susceptibility Throughout the $V$ - $T$ Plane

To explore the relationship between thermal and mechanical stimulation of the solid  $^4\text{He}$  sample revealed by  $f(T, V)$  and  $D(T, V)$ , we compare the rotational dynamics versus  $T$  as  $V \rightarrow 0$  to those versus  $V^{0.5}$  as  $T \rightarrow 0$ . Figures 5A and 5C show  $f(T)|_{V \rightarrow 0}$  and  $D(T)|_{V \rightarrow 0}$  while Figs. 5B and 5D show  $f(V)|_{T \rightarrow 0}$  and  $D(V)|_{T \rightarrow 0}$ . This shows an unexpected similarity between the results of what, for a simple superfluid, would be two distinct experiments—one stimulating the sample thermally and

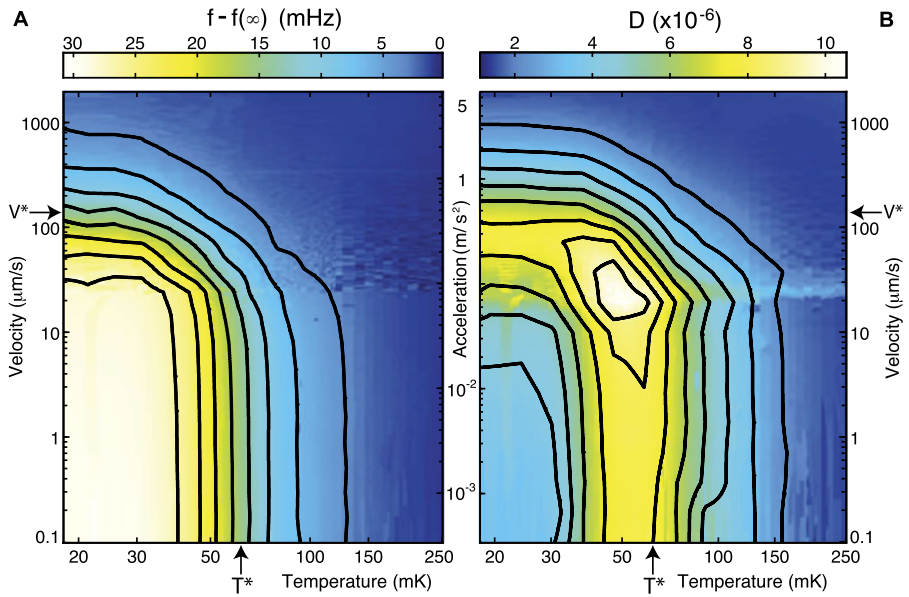


**Fig. 4** (A) TO resonant frequency shift  $f(T)$  and (B) dissipation data mapped throughout the  $V$ – $T$  plane. Ninety eight FID curves (each at a different temperature) were smoothly interpolated into the two color-coded surfaces displayed here on identical log-log axes. The low-velocity maximum frequency shift ( $\sim 33$  mHz) would correspond to a superfluid fraction of 5.6 % (Color figure online)

the other mechanically. To examine this effect, we defined an empirical measure  $\tau_E$  of relaxation times for any combination of  $T$  and  $V$  (see Eq. (5)):

$$\tau_E(T, V) = \frac{D(T, V)f(0)}{2\omega_0(f(0) - f(T, V))}. \tag{7}$$

In Fig. 5E we show  $\log \tau_E(T)$  plotted versus  $\log(T/T^*)$  for the lowest rim-velocity data (Figs. 5A, C). In Fig. 5F,  $\log \tau_E(V)$  is likewise plotted versus  $\log(V/V^*)$  for the lowest temperature data (Figs. 5B, D). Here we define  $T^*$  and  $V^*$  as the temperature and rim-velocity respectively at which half the total frequency shift has occurred (Figs. 4, 5A, 5B). This analysis reveals that the  $\tau_E$  diverge smoothly as  $T^\zeta$  with  $\zeta = -2.75 \pm 0.1$  when  $V \rightarrow 0$ , and as  $V^\lambda$  with  $\lambda = -1.17 \pm 0.05$  when  $T \rightarrow 0$ . Thus, the effects of temperature on  $f(T)|_{V \rightarrow 0}$  and  $D(T)|_{V \rightarrow 0}$  appear identical to those of rim-velocity on  $f(V^\gamma)|_{T \rightarrow 0}$  and  $D(V^\gamma)|_{T \rightarrow 0}$  respectively, where  $\gamma = \lambda/\zeta = 0.43$  is the ratio of power-law exponents. Figures 5E, F also show that the peak in  $D$  is *always* canceled by the peak in  $|df/dT|$  to produce smoothly diverging functions  $\tau_E(T)|_{V \rightarrow 0}$  and  $\tau_E(V)|_{T \rightarrow 0}$ . Microscopic relaxational processes represented by  $\tau_E$  could be expected to change dramatically at a superfluid phase transition; a good example of this is seen in  $\tau_E(T)$  at the BKT superfluid phase transition of liquid  $^4\text{He}$  [64, 65] shown inset to Fig. 5E. However, no indications of such a sudden change signifying a supersolid  $T_c$  or  $V_c$  is observed in Figs. 5E, F. Instead,  $\tau_E$  exhibits everywhere the smooth divergence expected in  $\omega\tau = 1$  models.

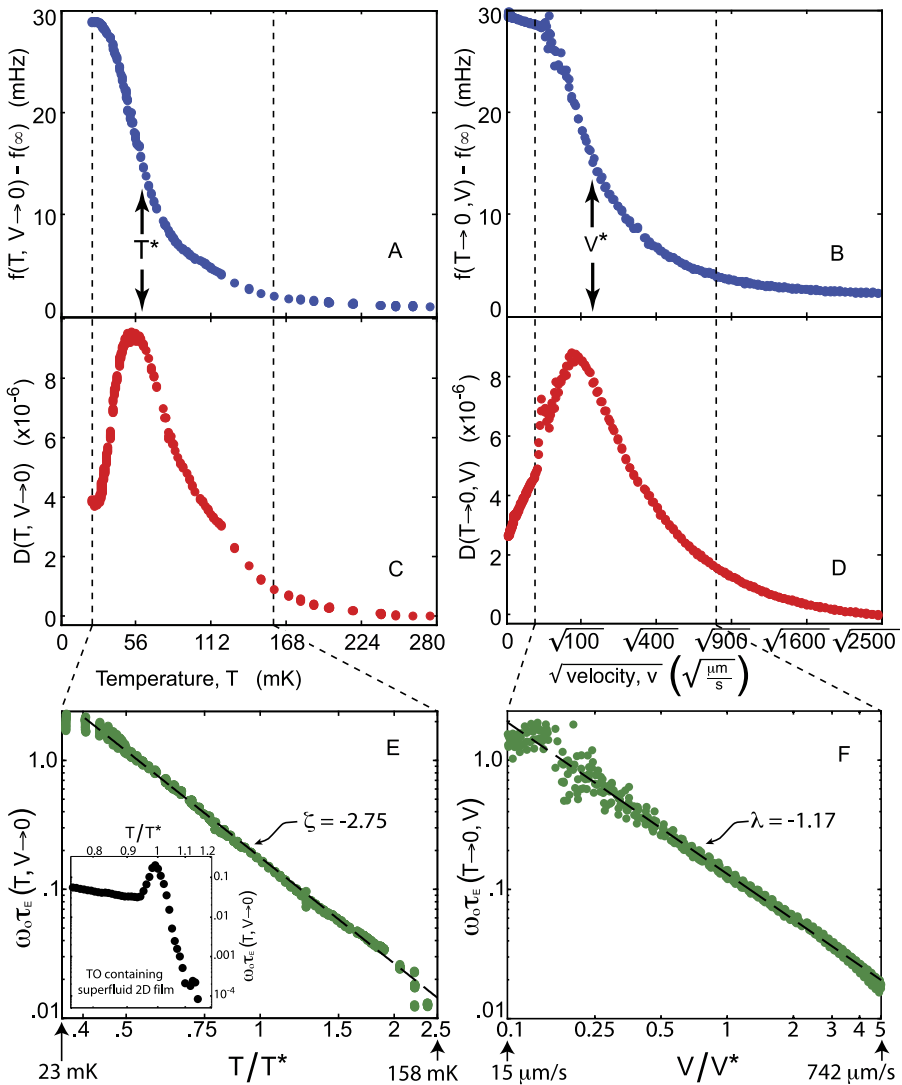


**Fig. 5** (A) TO resonant frequency shift  $f(T)$  measured at lowest rim-velocity.  $T^*$  is defined as the temperature at which 50 % of the frequency change has occurred (Fig. 4). (B) TO resonant frequency shift  $f(\sqrt{V})$  measured at lowest temperature.  $V^*$  is defined as the rim-velocity at which 50 % of the frequency change has occurred (Fig. 4). (C) TO dissipation  $D(T)$  measured at lowest rim-velocity. (D) TO dissipation  $D(\sqrt{V})$  measured at lowest temperature. (E) The empirical measure of microscopic relaxation times  $\omega_0 \tau_E(T)|_{V \rightarrow 0}$  from data in Figs. 5A, C. The inset shows the equivalent analysis using Eq. (7) for the BKT transition of a superfluid  $^4\text{He}$  film. (F) The empirical measure of microscopic relaxation times  $\omega_0 \tau_E(V)|_{T \rightarrow 0}$  from data in Figs. 5B, D (Color figure online)

### 7 Equivalence of Mechanical and Thermal Stimulation of Solid $^4\text{He}$

Figures 4 and 5 provide direct empirical evidence that the effects of  $T$  and  $V$  on the solid  $^4\text{He}$  within the TO are intimately related. One may then ask whether a sin-

gle rotational susceptibility could describe the whole  $V$ – $T$  plane dynamics in Fig. 4 when the effects of  $V$  on the relaxation time  $\tau$  are correctly incorporated. In attempting to explore this issue we make the simple hypothesis that the total microscopic relaxation rate  $1/\tau(T, V)$  is due to a combination of two effects

$$\frac{1}{\tau(T, V)} = \frac{1}{\tau(T)} + \frac{1}{\tau(V)}. \quad (8)$$

As the overall phenomenology appears identical as a function of  $T^\zeta|_{V \rightarrow 0}$  and  $V^\lambda|_{T \rightarrow 0}$  (Fig. 5) and interpolates smoothly between these limits (Fig. 4) the ansatz:

$$\frac{1}{\tau(T, V)} = \frac{\Sigma}{T^\zeta} + \frac{\Lambda}{V^\lambda} \quad (9)$$

is natural. Here  $\Sigma$  and  $\Lambda$  quantify the relative contributions to the relaxation rate from thermally and mechanically stimulated excitations. Figure 6A shows that by using this ansatz, all the complex solid  $^4\text{He}$  rotational dynamics in  $f(T, V)$  and  $D(T, V)$  shown in Fig. 4 can be collapsed onto just two functions  $\text{Re}(\chi^{-1})$  and  $\text{Im}(\chi^{-1})$  merely by plotting  $f[(T^*/T)^\zeta + (V^*/V)^\lambda]$  and  $D[(T^*/T)^\zeta + (V^*/V)^\lambda]$ . This collapse implies, further, that Eq. (7) could yield a comprehensive image of  $\tau_E(T, V)$  throughout the  $V$ – $T$  plane by dividing all the data in Fig. 4B by that in Fig. 4A, as shown in Fig. 6B. Here, although the proposed  $V$ – $T$  ranges for a supersolid phase transition [8, 9, 19] are at or below the dashed  $T^*$ – $V^*$  contour, the  $\tau_E$  surface exhibits everywhere the smoothly diverging relaxation processes expected in  $\omega_0\tau = 1$  models. We emphasize that all the above empirical results (Figs. 4–6) are independent of the choice of  $\chi_{^4\text{He}}^{-1}(T, V)$ .

## 8 Relating Solid $^4\text{He}$ Shear Dynamics to the Rotational Susceptibility

Measurements of the shear modulus  $\mu$  of solid  $^4\text{He}$  by Day and Beamish [32] revealed that the temperature dependence of the shear modulus  $\mu(T)$  is highly similar to the temperature dependence of the frequency  $f(T)$  measured in TO's. They also observed a corresponding dissipation peak in the shearing experiments [32]. Furthermore, they discovered that  $\mu$  has the same dependence on the amplitude of shear strain  $\varepsilon$ ,  $^3\text{He}$  concentration, and annealing as does the TO frequency  $f$  on rim-velocity,  $^3\text{He}$  concentration, and annealing [32]. Because the solid  $^4\text{He}$  shear modulus  $\mu(T)$  exhibits a very similar temperature dependence to  $f(T)$  [32], and because this shear stiffening effect is extinguished by a characteristic strain as opposed to a critical velocity [34], a key issue is whether the microscopic excitations generated by direct shearing are the same as those controlling the TO dynamics. Our approach provided a new opportunity to directly examine this issue. Figures 4 and 5 provide evidence that identical microscopic excitations are being generated by thermal and mechanical stimulation, and that the overall rotational dynamics in  $f(V, T)$  and  $D(V, T)$  are consistent with a single  $\omega_0\tau = 1$  mechanism that is controlled by a relaxation rate  $(T^*/T)^\zeta + (V^*/V)^\lambda$  due to the combined influences from these two sources (Fig. 6). If excitations induced by inertial strain  $\varepsilon$  in the TO (where  $\varepsilon \propto V$ ) are the cause of the anomalous rotational dynamics, then the indistinguishable structure of

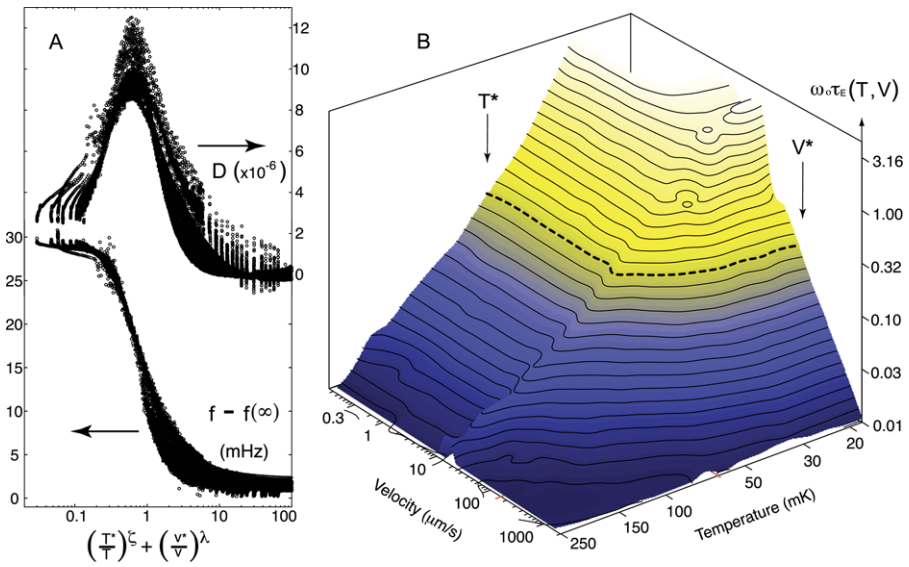


**Fig. 6** (A) All of the TO dynamical responses throughout the  $V$ - $T$  plane ( $f(T, V)$  from Fig. 4A and  $D(T, V)$  from Fig. 4B) are collapsed onto just two curves (very similar in structure to the  $\text{Re}(\chi^{-1})$  and  $\text{Im}(\chi^{-1})$  components of the Debye susceptibility) by plotting  $f[(T^*/T)^\zeta + (V^*/V)^\lambda]$  and  $D[(T^*/T)^\zeta + (V^*/V)^\lambda]$ . Here we find that  $\text{Re}(\chi^{-1}) \propto f[(T^*/T)^\zeta + (V^*/V)^\lambda]$  is always too large in comparison to  $\text{Im}(\chi^{-1}) \propto D[(T^*/T)^\zeta + (V^*/V)^\lambda]$  to be explained quantitatively by a Debye susceptibility model; this point has been used to motivate a “superglass” hypothesis [14]. (B) A comprehensive map of empirical relaxation times  $\omega_0 \tau_E(T, V)$  deduced using Eq. (7) represented as a surface in the  $\log T$ - $\log V$  plane. The equally-spaced contour lines in  $\log \omega_0 \tau_E(T, V)$  reveal the underlying divergence of  $\omega_0 \tau_E(T, V)$  as combined power laws  $[(T^*/T)^\zeta + (V^*/V)^\lambda]$  (Color figure online)

$f(T)|_{V \rightarrow 0}$  and  $f(V^\nu)|_{T \rightarrow 0}$  (Fig. 7A) should be mirrored by an equivalently indistinguishable relationship in shear modulus between  $\mu(T)|_{\varepsilon \rightarrow 0}$  and  $\mu(\varepsilon^\nu)|_{T \rightarrow 0}$ . When the measured  $\mu$  from Ref. [34] is plotted simultaneously versus  $T$  and  $\varepsilon^\nu$  in Fig. 7B (using the power-law ratio  $\nu$  derived from our TO studies), this is what we find. That the combined temperature-velocity dependence of the TO response mirrors quantitatively the combined temperature-strain dependence of the shear modulus, along with the original observation that  $\mu(T)$  tracks  $f(T)$  [32], implies strongly that the rotational dynamics of solid  $^4\text{He}$  are closely associated with the generation (presumably by inertial shearing) of the same type of microscopic excitations which are generated by direct shear strain  $\varepsilon$ . These deductions are also in good accord with the absence of any signature in estimated relaxation times  $\tau_E(T, V)$  for the  $T_c$  or  $V_c$  of the proposed supersolid phase transition (Figs. 5, 6), and the associated observation of the universal smoothly diverging  $\tau_E(T, V)$  expected in  $\omega\tau = 1$  models.

### 9 Conclusions and Future

In this paper we described the development and implementation of novel high-precision and high-data-volume techniques for TO studies of solid  $^4\text{He}$ . Our DC-

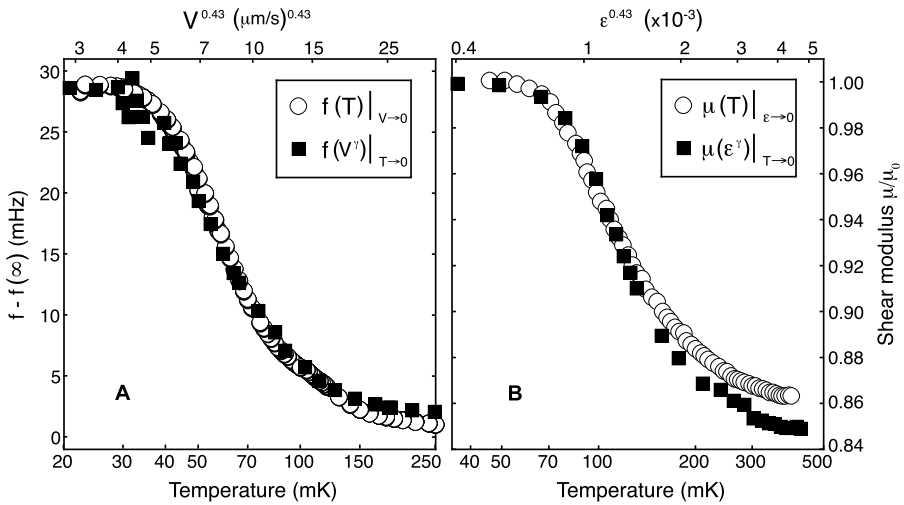


**Fig. 7** (A) Plots of our simultaneously measured  $f(T)|_{V \rightarrow 0}$  (open circles) and  $f(V^V)|_{T \rightarrow 0}$  (filled squares) from Figs. 4 and 5. (B) Simultaneous plots of measured  $\mu(T)|_{\varepsilon \rightarrow 0}$  (open circles) and  $\mu(\varepsilon^V)|_{T \rightarrow 0}$  (filled squares) from Ref. [34] acquired at 2000 Hz

SQUID-based TO system allows unprecedented sensitivity and dynamic range making the free inertial decay technique viable, and yielded the first comprehensive map of  $f(T, V)$  and  $D(T, V)$  for solid  $^4\text{He}$ . Our introduction of the generalized rotational susceptibility  $\chi_{^4\text{He}}^{-1}(\omega, T)$  technique also allows an unbiased approach to studying solid  $^4\text{He}$  rotational dynamics. Moreover, a specific model for  $\chi_{^4\text{He}}^{-1}(\omega, \tau(T))$  in which  $\tau(T)$  represents the relaxation rate for inertially active microscopic excitations provides an intuitively satisfying model for why  $df/dT$  and  $D$  pass simultaneously through a maximum when  $\omega\tau(T^*) = 1$ . Our studies reviewed here have all been carried out in the context of these new approaches to the solid  $^4\text{He}$  problem.

Solid  $^4\text{He}$  sample characteristics are notoriously non-universal. And indeed, in our studies, we found that equilibration times within  $f(T)$  and  $D(T)$  exhibit a complex synchronized ultraslow evolution toward equilibrium indicative of uncontrolled glassy freezing of crystal disorder conformations. During this slowing down, the synchronized relationship of  $\text{Re}(\chi_{^4\text{He}}^{-1})$  to  $\text{Im}(\chi_{^4\text{He}}^{-1})$  is always retained, meaning that each precise crystal disorder conformation strongly influences the rotational dynamics. Such slow conformation changes linked to rotational dynamics are actually endemic to studies of solid  $^4\text{He}$  and are manifested variously as hysteresis effects [11, 36], annealing effects [10, 23, 28–31], and glassy dynamics [14, 30, 61, 62].

However, once a given disorder conformation has been stabilized (the situation in which most solid  $^4\text{He}$  studies are presumed to be carried out) we found that analysis of  $\chi_{^4\text{He}}^{-1}(\omega, \tau(T, V))$  provides evidence that microscopic excitations controlling the TO motions are generated independently by thermal and mechanical stimulation of the crystal. Moreover, a measure for their relaxation times  $\tau(T, V)$  diverges smoothly everywhere, as expected in  $\omega\tau = 1$  models with no indication whatsoever of a thermodynamic transition. Finally, the combined temperature-velocity dependence of the TO response is indistinguishable from the combined temperature-strain dependence

of the  $^4\text{He}$  shear modulus—directly linking the shearing characteristics to the TO effects.

Overall, our observations imply that ultra-slow equilibration of crystal disorder conformations continues to evolve even at lowest temperatures in solid  $^4\text{He}$ . Then, for any given disorder conformation, the rotational responses of solid  $^4\text{He}$  are associated with generation of the same microscopic excitations as those produced by direct shear strain. If superfluidity is the correct interpretation of the blocked annulus experiments [9, 17], then one hypothesis consistent with all these observations is that amorphous low temperature solid  $^4\text{He}$  is a ‘superglass’—a state in which dynamical excitations within the solid control the superfluid phase stiffness. A key experiment to test this hypothesis would use a variable frequency oscillator to measure the frequency dependent rotational susceptibility. Firstly, by severely constraining theoretical models, such a susceptibility would help identify if these microscopic excitations are crystal dislocations as implied. Secondly, if a superfluid component does exist, then the real and imaginary parts of this susceptibility would not satisfy the Kramers-Kronig relations.

**Acknowledgements** We acknowledge and thank J. Beamish, D.M. Ceperley, M.W.H. Chan, A. Clark, J. Day, A. Dorsey, R.B. Hallock, H. Kojima, D.M. Lee, A.J. Leggett, E. Mueller, S. Nagel, D.R. Nelson, M. Paalanen, J. Parpia, N.V. Prokof’ev, J.D. Reppy, J. Saunders, J.P. Sethna, P.C.E. Stamp, B. Svistunov, and M. Troyer. These studies are supported by the National Science Foundation under grants DMR-0806629 and NSF PHY05-51164 (KITP); Work at Los Alamos was supported by U.S. Department of Energy grant DE-AC52-06NA25396 through LDRD.

## References

1. D. Thouless, *Ann. Phys.* **52**, 403 (1969)
2. A.F. Andreev, I.M. Lifshitz, *Sov. Phys. JETP* **29**, 1107 (1969)
3. L. Reatto, *Phys. Rev.* **183**, 334 (1969)
4. G.V. Chester, *Phys. Rev. A* **2**, 256 (1970)
5. A.J. Leggett, *Phys. Rev. Lett.* **25**, 1543 (1970)
6. M.W. Meisel, *Physica B* **178**, 121 (1992)
7. S. Balibar, *Nature* **464**, 176–182 (2010)
8. E. Kim, M.H.W. Chan, *Nature* **427**, 225–227 (2004)
9. E. Kim, M.H.W. Chan, *Science* **305**, 1941–1944 (2004)
10. A.S.C. Rittner, J.D. Reppy, *Phys. Rev. Lett.* **97**, 165301 (2006)
11. Y. Aoki, J.C. Graves, H. Kojima, *Phys. Rev. Lett.* **99**, 015301 (2007)
12. A. Penzev, Y. Yasuta, M. Kubota, *J. Low Temp. Phys.* **148**, 677–681 (2007)
13. M. Kondo, S. Takada, Y. Shibayama, K. Shirahama, *J. Low Temp. Phys.* **148**, 695–699 (2007)
14. B. Hunt et al., *Science* **324**, 632–636 (2009)
15. E.J. Pratt et al., *Science* **332**, 821–824 (2011)
16. H. Choi, S. Kwon, D.Y. Kim, E. Kim, *Nat. Phys.* **6**, 424–427 (2010)
17. A.S.C. Rittner, J.D. Reppy, *Phys. Rev. Lett.* **101**, 155301 (2008)
18. D.R. Tilley, J. Tilley, *Superfluidity and Superconductivity*, 3rd edn. (IOP, Bristol, 1990)
19. X. Lin, A.C. Clark, M.H.W. Chan, *Nature* **449**, 1025–1028 (2007)
20. X. Lin, A.C. Clark, Z.G. Cheng, M.H.W. Chan, *Phys. Rev. Lett.* **102**, 125302 (2009)
21. J.-J. Su, M.J. Graf, A.V. Balatsky, *J. Low Temp. Phys.* **159**, 431–440 (2010)
22. J. Day, J. Beamish, *Phys. Rev. Lett.* **96**, 105304 (2006)
23. S. Sasaki, R. Ishiguro, F. Caupin, H.J. Maris, S. Balibar, *Science* **313**, 1098–1100 (2006)
24. M.W. Ray, R.B. Hallock, *Phys. Rev. Lett.* **100**, 235301 (2008)
25. M.W. Ray, R.B. Hallock, *Phys. Rev. B* **79**, 224302 (2009)
26. M.W. Ray, R.B. Hallock, *Phys. Rev. B* **82**, 012502 (2010)

27. M.W. Ray, R.B. Hallock, *Phys. Rev. B* **84**, 144512 (2011)
28. A.S.C. Rittner, J.D. Reppy, *Phys. Rev. Lett.* **98**, 175302 (2007)
29. A.C. Clark, J.T. West, M.H.W. Chan, *Phys. Rev. Lett.* **99**, 135302 (2007)
30. A.C. Clark, J.D. Maynard, M.H.W. Chan, *Phys. Rev. B* **77**, 184513 (2008)
31. S. Sasaki, F. Caupin, S. Balibar, *Phys. Rev. Lett.* **99**, 205302 (2007)
32. J. Day, J. Beamish, *Nature* **450**, 853–856 (2007)
33. O. Syshchenko, J. Day, J. Beamish, *Phys. Rev. Lett.* **104**, 195301 (2010)
34. J. Day, O. Syshchenko, J. Beamish, *Phys. Rev. Lett.* **104**, 075302 (2010)
35. P.W. Anderson, *Nat. Phys.* **3**, 160–162 (2007)
36. A. Penzev, Y. Yasuta, M. Kubota, *Phys. Rev. Lett.* **101**, 065301 (2008)
37. S.I. Shevchenko, *Sov. J. Low Temp. Phys.* **13**, 61–69 (1987)
38. M. Boninsegni et al., *Phys. Rev. Lett.* **99**, 035301 (2007)
39. J. Wu, P. Phillips, *Phys. Rev. B* **78**, 014515 (2008)
40. J. Bossy, J.V. Pearce, H. Schober, H.R. Glyde, *Phys. Rev. B* **78**, 224507 (2008)
41. G. Biroli, C. Chamon, F. Zamponi, *Phys. Rev. B* **78**, 224306 (2008)
42. B. Svistunov, *Physica B* **404**, 521–523 (2009)
43. K.-M. Tam, S. Geraedts, S. Inglis, M.J.P. Gingras, R.G. Melko, *Phys. Rev. Lett.* **104**, 215301 (2010)
44. X. Rojas, A. Haziot, V. Bapst, S. Balibar, H.J. Maris, *Phys. Rev. Lett.* **105**, 145302 (2010)
45. A.V. Balatsky, M.J. Graf, Z. Nussinov, S.A. Trugman, *Phys. Rev. B* **75**, 094201 (2007)
46. Z. Nussinov, A.V. Balatsky, M.J. Graf, S.A. Trugman, *Phys. Rev. B* **76**, 014530 (2007)
47. M.J. Graf, Z. Nussinov, A.V. Balatsky, *J. Low Temp. Phys.* **158**, 550–559 (2010)
48. A.F. Andreev, *JETP Lett.* **85**, 585–587 (2007)
49. I. Iwasa, *Phys. Rev. B* **81**, 104527 (2010)
50. J.-J. Su, M.J. Graf, A.V. Balatsky, *Phys. Rev. Lett.* **105**, 045302 (2010)
51. J.-J. Su, M.J. Graf, A.V. Balatsky, *J. Low Temp. Phys.* **162**, 433–440 (2011)
52. J.-J. Su, M.J. Graf, A.V. Balatsky, *New J. Phys.* **13**, 113024 (2011)
53. S.E. Korshunov, *JETP Lett.* **90**, 156–159 (2009)
54. K.S. Cole, R.H. Cole, *J. Chem. Phys.* **9**, 341 (1941)
55. D.W. Davidson, R.H. Cole, *J. Chem. Phys.* **19**, 1484 (1951)
56. S.V. Pereverzev, A. Loshak, S. Backhaus, J.C. Davis, R.E. Packard, *Nature* **388**, 449–451 (1997)
57. E. Hoskinson, Y. Sato, I. Hahn, R.E. Packard, *Nat. Phys.* **2**, 23–26 (2006)
58. J. Clarke, A. Braginski (eds.), *The SQUID Handbook*, vol. 1 (Wiley-VCH, Weinheim, 2004)
59. H.J. Paik, *J. Appl. Phys.* **47**, 1168–1178 (1976)
60. Quantum Design, model 550
61. Y. Aoki, M.C. Keiderling, H. Kojima, *Phys. Rev. Lett.* **100**, 215303 (2008)
62. V.N. Grigor'ev et al., *Phys. Rev. B* **76**, 224524 (2007)
63. A.A. Lisunov et al., *Phys. Rev. B* **83**, 132201 (2011)
64. D.J. Bishop, J.D. Reppy, *Phys. Rev. Lett.* **40**, 1727–1730 (1978)
65. V. Ambegaokar, B.I. Halperin, D.R. Nelson, E.D. Siggia, *Phys. Rev. B* **21**, 1806–1826 (1980)